International Journal of Heat and Fluid Flow 66 (2017) 83–94

Contents lists available at ScienceDirect

International Journal of Heat and Fluid Flow

journal homepage: www.elsevier.com/locate/ijhff

Skin-friction drag reduction in a channel flow with streamwise-aligned plasma actuators

O. Mahfoze, S. Laizet*

Department of Aeronautics, Imperial College London, London, SW7 2AZ, UK

ARTICLE INFO

Article history:
Received 9 January 2017
Revised 28 April 2017
Accepted 1 May 2017

Keywords:
Plasma actuators
Direct numerical simulation
Skin-friction drag reduction
Turbulence

ABSTRACT

Direct Numerical Simulations in a turbulent channel flow at a moderate Reynolds number are performed in order to investigate the potential of Dielectric Barrier Discharge (DBD) plasma actuators for the reduction of the skin-friction drag. The idea is to use a sparse array of streamwise-aligned plasma actuators to produce near-wall spanwise-orientated jets in order to destroy the events which transport high-speed fluid towards the wall. It is shown that it is possible to reduce the drag by about 33.5% when the streamwise-aligned actuators are configured to generate appropriate spanwise-orientated jets very close to the wall so that the sweeps which are mainly responsible for the skin-friction are destroyed. We demonstrate that it is possible to achieve significant drag reduction with a sparse array of streamwise-aligned plasma actuators, with one order of magnitude less actuators than previous experiments in a similar set-up.

1. Introduction

One of the most challenging tasks for turbulent flows is how to achieve skin-friction drag reduction due to an evident practical significance for engineering applications and related global impact on the sustainability challenges that we are facing today. It is now well-established that skin-friction drag reduction requires a disruption and weakening of the large-scale wall-normal motions that are associated with quasi-streamwise vortices, responsible for the formation of alternately high-speed and low-speed streaks near the wall (Virk, 1975; Kravchenko et al., 1993; Orlandi and Jiménez, 1994; Touber and Leschziner, 2012). In the last few decades, fundamental research efforts in skin-friction drag reduction have had a considerable success, and several viable strategies to reduce drag have been introduced, although often only proofs-of-concept based on numerical simulations or laboratory experiments are available. In particular, spanwise oscillation is one of the most effective techniques in wall-turbulence control, with as much as 45% reduction in skin-friction drag observed in the literature. Many experimental and numerical studies have been performed to examine the underlying mechanisms responsible for drag reduction by spanwise oscillations (Bradshaw and Pontikos, 1985; Moin et al., 1990; Choi et al., 1998; Jukes et al., 2006; Touber and Leschziner, 2012). It was shown in those studies that imposing a constant transverse strain near the wall can progressively reduce the turbulent kinetic energy, Reynolds stresses and associated skin-friction drag. The authors in Choi et al. (2002) argued that negative spanwise vorticity are produced as a result of wall oscillations, thereby modifying the vortex-stretching mechanism responsible for the production of turbulence. Experiments in a water channel demonstrated that the near-wall flow is dragged laterally by wall oscillations, with a reduction of the length of the streaks and an increase of the spacing between them (Ricco, 2004). More recently it was shown numerically that wall oscillations are strongly altering the near-wall streaks and are reducing the contribution of turbulence to the wall shear stress (Touber and Leschziner, 2012).

There are a mainly two different strategies to achieve spanwise oscillations. The first option is to enforce the oscillations by directly imposing an oscillatory motion for the wall (Choi et al., 1998; Quadrio and Ricco, 2004; Touber and Leschziner, 2012). The second option is to use actuators to modify the flow very close to the wall. Several methods are available such as electro-magnetic (Lorentz force) oscillation (Berger et al., 2000; Du et al., 2002; Pang and Choi, 2004), local oscillatory blowing (Tardu, 2001; Segawa et al., 2007) and plasma actuators (Jukes et al., 2006; Choi et al., 2011; Whalley and Choi, 2014). All of these methods result in a similar amount of drag reduction for low Reynolds numbers turbulent flows. Actually, the authors in Iwamoto et al. (2002) showed numerically that the performance of skin-friction drag reduction techniques is gradually deteriorated when the Reynolds number is

* Corresponding author.
E-mail address: s.laizet@imperial.ac.uk (S. Laizet).

http://dx.doi.org/10.1016/j.ijheatfluidflow.2017.05.013

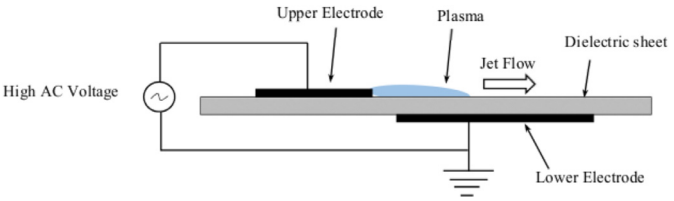

Fig. 1. Schematic diagram of an asymmetric DBD plasma actuator.

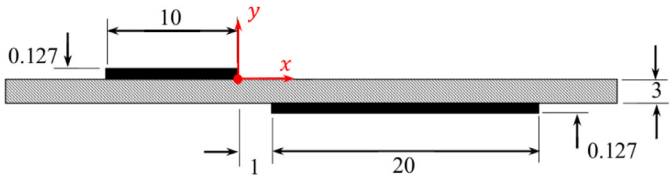

Fig. 2. Sketch of the plasma actuator used in the experiments of Benard et al. (2015). The dimension are in mm (not to scale).

increased. However, it was estimated theoretically that it should be possible to achieve a substantial drag reduction at very high Reynolds numbers (of the order of 10^5), providing that you can remove the turbulence from the buffer layer to the wall (Iwamoto et al., 2005). Finally, it should be noted that there is an open issue concerning the global energetic balance of the oscillating wall as a skin-friction drag reduction technique. The external power required to induce the spanwise oscillations can be one order of magnitude larger than the power saved owing to the skin-friction drag reduction (Quadrio and Ricco, 2004). On the positive side, it was demonstrated that net energy savings of the order of 10% are possible for low wall-oscillation velocities and low Reynolds numbers (Baron and Quadrio, 1995; Jung et al., 1992).

Following the experiments of Jukes et al. (2006), Choi et al. (2011) and Whalley and Choi (2014) the present study aims to investigate numerically a skin-friction drag reduction technique based on dielectric barrier discharge (DBD) plasma actuators. The main advantages in using these actuators are their special features that include being fully electronic with no moving parts, a fast time response for unsteady applications, a very low mass and a low power consumption. DBD plasma actuators consist of two electrodes, one exposed to the ambient fluid and the other covered by a dielectric material as shown in Fig. 1. The two electrodes are supplied with an A.C. voltage which causes the ambient fluid over the covered electrode to ionize. This ionized fluid is called the plasma and results in a body force vector which exchanges momentum with the ambient, neutrally charged, fluid. In a quiescent fluid, a DBD plasma actuator creates an induced flow towards the edge of the exposed electrode in the direction of the covered electrode and a jetting of the flow towards the far edge of the covered electrode. Extensive reviews of plasma actuators for aerodynamic applications can be found in Moreau (2007) and Corke et al. (2010). When streamwise-aligned in opposing pairs (see Fig. 7), DBD plasma actuators can be used to generate oscillating wall-jets very close to the wall, mimicking the effect of spanwise wall oscillations (Jukes et al., 2006; Choi et al., 2011; Whalley and Choi, 2014).

The first objective of the present study is to reproduce numerically, with a simple phenomenological model, the underlying physics responsible for the skin-friction drag reduction observed in the experiments of Jukes et al. (2006), Choi et al. (2011) and Whalley and Choi (2014) in a turbulent boundary layer at a moderate Reynolds number. In order to minimise the energy input, the second objective is to design a sparse array of actuators by comparison to the experiments of Jukes et al. (2006), Choi et al. (2011) and Whalley and Choi (2014), with a reduction of the number of streamwise-aligned plasma actuators by at least by one order of magnitude, while still achieving a significant drag reduction.

The organisation of the paper is as follows. First, we describe and compare three different phenomenological models used to generate a forcing term in the Navier–Stokes equations to reproduce the effect of DBD plasma actuators on the ambient fluid. Then we implement the model in our high-order flow solver and compare the effect of streamwise-aligned DBD plasma actuators in a fluid at rest with the experimental data of Jukes et al. (2006), Choi et al. (2011) and Whalley and Choi (2014). Drag reduction investigations are then carried out with pairs of streamwise-aligned actuators with and without spanwise oscillations. The underlying mechanisms for drag reduction are discussed thanks to 2D and 3D instantaneous snapshots of the flow as well as with virtual probes and the VITA technique. The paper is ended with a discussion about power balance and a conclusion.

2. Modelisation of DBD plasma actuators

Attempts at modelling DBD plasma actuators can be divided into two groups: first-principle based models and simplified phenomenological models. The first-principle based models are aiming at modelling the physical mechanisms of the actuator. They require the solution of complex transport equations for both charged and neutral species and a Poisson equation for the electric field. They are very expensive and can cost up to several orders of magnitude more than simplified models (Boeuf et al., 2007; Singh and Roy, 2008; Rogier et al., 2014; Parent et al., 2016; Nishida et al., 2014; 2016).

Simplified phenomenological models attempt to capture the ionization effects of the plasma actuator without directly modelling the species transport equations. Those models are based on the assumption that the plasma formation and fluid flow response can be decoupled due to the large disparities in the characteristic velocities associated with each process (Mertz and Corke, 2011). Among the most popular of those models are the Shyy model (Shyy et al., 2002) and the Suzen & Huang models (Suzen et al., 2005; 2007) because of their relative simplicity and ability to mimic the time-averaged effects of a DBD actuator on the ambient fluid. Even if those models are time-independent, they are widely used and have been validated in a turbulent channel flow (Ibrahim and Skote, 2014; Li et al., 2015) for single spanwise-aligned actuators.

Because this is the first attempt to achieve numerically drag reduction using streamwise-aligned pairs of plasma actuators in a turbulent channel flow, simplicity and easiness of implementation are essential starting points. Our objective here is to be able to generate spanwise-orientated jets close to the wall and this can be achieved without expensive first-principle based models. In this section, three DBD plasma actuator models among the most popular simplified phenomenological ones are tested and validated against the experimental data of Benard et al. (2015): The Shyy model (Shyy et al., 2002) (Shy02), the Suzen and Huang model of 2005 (Suzen et al., 2005) (S&H05), and the Suzen and Huang Model of 2007 (Suzen et al., 2007) (S&H07). The dimensions of the plasma actuator to be modelled are indicated in Fig. 2. The plasma actuator is made of a 10 mm air-exposed and a 20 mm grounded electrode (with an inter-electrode distance of 1 mm), these two electrodes are placed on both side of a 3 mm thick PMMA plate acting as dielectric barrier. The reference experimental time-averaged velocity profiles were obtained in an ambient fluid at rest, at the spanwise centre of the actuator with an applied voltage V_{rms} equals to 20 kV, and an applied frequency of 1000 Hz. More details about the experimental set-up can be found in Benard et al. (2015).

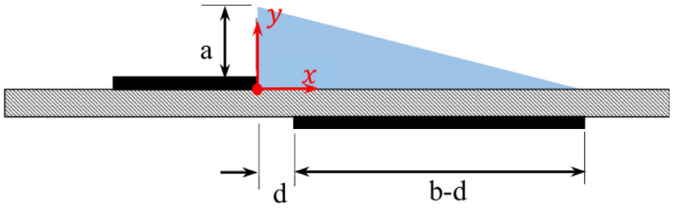

Fig. 3. Linearised plasma shape of the Shyy02 model.

2.1. Shyy02 model

The Shyy model is very simple model to estimate the influence of a DBD plasma actuator on the ambient fluid. It assumes that the electrical field strength decays linearly along the dielectric material from the end of the upper electrode to the end of the lower electrode. The plasma forcing term is approximated as a triangle as shown in Fig. 3. The body force **f**, to be added in the Navier–Stokes equations as an extra term in the momentum equation, is defined as

$$\mathbf{f} = f_{AC}\Delta t \rho_c e_c \delta \mathbf{E} \tag{1}$$

where f_{AC} is the applied voltage frequency, Δt is the discharge time, ρ_c is the discharge density, e_c is the electron charge, δ is a switch function (equals 1 inside the forcing area and to 0 outside) and **E** is the electrical field. The magnitude of the electrical field E is calculated by the following linear equation

$$|E| = E_0 - k_1 x - k_2 y. \tag{2}$$

If d is defined as the gap between the exposed electrode and the embedded electrode, then the maximum electrical field between the two electrodes E_0 is approximated as V_{rms}/d where V_{rms} corresponds to the rms of the applied voltage. The parameters k_1 and k_2 are given by

$$k_1 = \frac{E_0 - E_b}{b} \qquad k_2 = \frac{E_0 - E_b}{a} \tag{3}$$

where E_b is the breakdown electric field strength (Capitelli et al., 2013). The electrical field **E** can be decomposed into a time-averaged wall-parallel component E_x and a time-averaged wall-normal component E_y

$$E_x = \frac{Ek_2}{\sqrt{k_1^2 + k_2^2}} \qquad E_y = \frac{Ek_1}{\sqrt{k_1^2 + k_2^2}} \tag{4}$$

The various parameters required for the forcing term to model the plasma actuator considered here are: $\rho_c = 1.0 \times 10^{11}$ C/m^3, $e_c = 1.60217662 \times 10^{-19}$ C, $E_b = 30$ kV/cm, $\Delta t = 67$ μs, $a = 8$ mm, $b = 21$ mm and $d = 1$ mm.

2.2. S&H05 model

The body force **f** is generated from the solution of a Laplace's equation for the electric potential due to the voltage applied to the electrodes and a Poisson-like second order partial differential equation for the charge density of the ionized working fluid. The derivation starts with the assumption that the magnetic force is negligible and the body force can be expressed as

$$\mathbf{f} = \rho_c \mathbf{E}. \tag{5}$$

Assuming further that the time variation of the magnetic field can be neglected, Maxwell's equation then states that the electric field **E** is conservative, allowing it to be expressed in terms of the gradient of a scalar potential ($\mathbf{E} = -\nabla\Phi$). Using Gauss's law ($\nabla \cdot \mathbf{E} = \rho/\varepsilon_0$), we get

$$\nabla \cdot (\varepsilon \nabla \Phi) = -\rho_c. \tag{6}$$

Assuming that the charge above the embedded electrode does not extend far and that the gas particles are weakly ionized, the potential Φ is split into ϕ, the electric potential due to the external electric field and φ, the electric potential due to the net charge density. For this particular model, the extend of the charge above the embedded electrode is controlled by the Debye length λ_d, which is the characteristic length for electrostatic shielding in plasma and is typically on the order of 10^{-4} m for gas discharge at atmospheric conditions (Roth, 1995; Suzen et al., 2007). Eq. (6) can be replaced by two separate equations, which also introduce the relative permittivity properties ε_r of the working fluid and plasma actuator materials

$$\nabla \cdot (\varepsilon_r \nabla \phi) = 0 \tag{7}$$

$$\nabla \cdot (\varepsilon_r \nabla \varphi) = -(\rho_c/\varepsilon_0). \tag{8}$$

Using the equation describing the net charge density in a plasma, a relationship between φ and ρ_c can be established as follow

$$\varphi = (-\rho_c \lambda_d^2/\varepsilon_0). \tag{9}$$

This allows Eq. (8) to be re-written into its final form as an equation for the charge density itself

$$\nabla \cdot (\varepsilon_r \nabla \rho_c) = \rho_c/\lambda_d^2. \tag{10}$$

Combining the results from Eqs. (7) and (10) the body force can be computed from

$$\mathbf{f} = \rho_c(-\nabla\phi). \tag{11}$$

Eqs. (7) and (10) do not contain any time dependent terms and can be normalised by their respective maximum input values, $\phi^{\max}$ corresponding to the maximum applied voltage and $\rho_c^{\max}$ corresponding to the specified maximum charge density. Thus the equations only have to be solved once at the beginning of a simulation or externally. In order to obtain the instantaneous body force the normalised electric potential and charge density are multiplied by their respective maximum values as well as a wave from function $f(t) = \sin(2\pi f_{AC} t)$. With ϕ^* and ρ^* denoting the normalised variables, the force can be computed from:

$$\mathbf{f} = (\phi^{max} f(t) \rho_c^{max} f(t)) \rho_c^*(\mathbf{x})(-\nabla\phi^*(\mathbf{x})) \tag{12}$$

For this model the potential and the discharge density equations are solved using the boundary conditions which are described in Fig. 4 (left). They assumed a Gaussian distribution of the discharge density on the dielectric surface above the embedded electrode $\rho_{c,w}(x) = \rho_c^{\max} G(x)$ with

$$G(x) = exp\left(\frac{-(x-\mu)^2}{2\sigma^2}\right). \tag{13}$$

μ is the location of the maximum discharge $\rho_c^{\max}$ (located at the corner of the embedded electrode closest to the exposed one) and σ is a scaling parameter defining the decay rate. Its important to note that these parameters, as well as the Debye length λ_d are obtained empirically.

2.3. S&H07 model

This model is based on the same approach as the S&H05 model. The only difference is that the boundary condition of the charge density ρ_c is simplified. It is assumed that the source of the charge density is the embedded electrode as seen in Fig. 4 (right). The Gaussian distribution σ on the surface is no longer needed. Hence, the unknown parameters are reduced to $\rho_c^{\max}$ and λ_d which are empirically evaluated thanks to the experimental data of Benard et al. (2015).

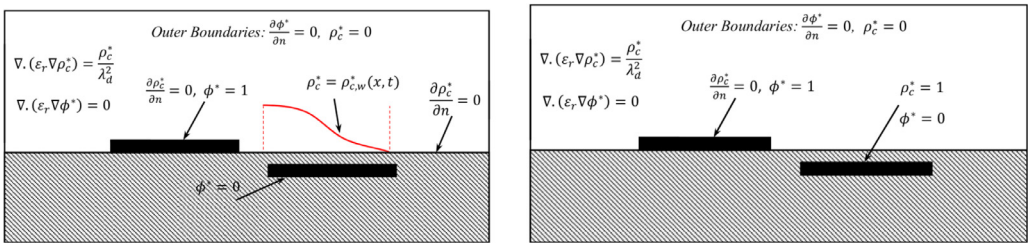

Fig. 4. Boundary conditions for the S&H05 model (left) and for the S&H07 model (right).

2.4. Navier–Stokes flow solver

The forcing term **f** generated to account for the effect of a DBD plasma actuator can be implemented into the high-order flow solver `Incompact3d`[1] as an extra forcing term in the incompressible Navier–Stokes equations

$$\frac{\partial \mathbf{u}}{\partial t} = -\nabla p - \frac{1}{2}[\nabla\cdot(\mathbf{u}\otimes\mathbf{u}) + (\mathbf{u}\cdot\nabla)\mathbf{u}] + \nu\nabla^2\mathbf{u} + \mathbf{f} \tag{14}$$

$$\nabla\cdot\mathbf{u} = 0 \tag{15}$$

where **u** is the velocity and p the pressure field. To solve these equations, finite-difference sixth-order compact schemes for spatial discretisation on a Cartesian mesh are used along with a third-order Adams–Bashforth scheme for time advancement. To treat the incompressibility condition, a fractional step method is required to solve a Poisson equation. For efficiency reasons, this equation is solved in spectral space using appropriate 3D Fast Fourier Transforms and with modified wave numbers in order to have a strict equivalence between all the operators. Note that the divergence free condition is ensured up to machine accuracy. When needed, a stretched mesh can be used in one direction in order to capture the small-scale dynamics with high fidelity. More details about the present code and its validation, especially the original treatment of the pressure in spectral space, can be found in Laizet and Lamballais (2009). For the 2D simulations performed for the comparison of the models, inflow/outflow boundary conditions are imposed in the streamwise direction ($x-$direction), zero-velocity boundary conditions are imposed in the vertical direction ($y-$direction) at the bottom of the computational domain while homogeneous Neumann boundary conditions are imposed at the top of the domain.

2.5. Comparison of the models

The simulations for the single plasma actuator of Fig. 2 in a fluid at rest are performed with $n_x \times n_y = 1024 \times 129$ mesh nodes on a domain $L_x \times L_y = 32l \times 8l$ where l is the reference length equal to 10 mm. The Reynolds number $Re = 3360$ is based on l and on $U_{\max} = 4.5$ m/s, which is the maximum velocity obtained in the experiments (Benard et al., 2015).

Several preliminary simulations have been performed in order to find the optimum parameters for the Shyy02, S&H05 and S&H07 models. The maximum discharge density $\rho_c^{\max}$ is defined such that the experimental trust is equal to the numerical one. The other parameters such as σ for the S&H05 model are obtained empirically. For the Shyy02 model, the plasma height a is varied from 2 to 10 mm, every 2 mm. The Debye length λ_d for the S&H05 and S&H07 models is tested in the range 1 mm–4.5 mm every 0.5 mm. The Gaussian distribution of the charge density σ for the S&H05 model is tested with three different values 0.1, 0.15 and 0.3 for each value of λ_d. To compare the simulations with the experimental data, a small script was designed to read the steady state velocity field from the simulation and to map it with the same resolution as the experimental velocity field. Point to point comparison and evaluation of the rms of the deviation from the experimental data were achieved. The optimised parameters are $a = 8$ mm for the Shyy02 model, $\lambda_d = 3.5$ mm and $\sigma = 0.3$ for the S&H05 model and $\lambda_d = 2.5$ mm for the S&H07 model.

Fig. 5 shows the time-averaged velocity profile U_x at 2.5 mm and 10 mm downstream of the end of the upper electrode obtained with the optimised parameters. At $x = 10$ mm, the three models are able to generate a laminar jet close to the wall with maximum speeds in the range 2.75 m/s–3.75 m/s, close to the maximum velocity of 4.05 m/s obtained in the experiments. It can be seen that, for this particular plasma actuator the best results are obtained with the S&H05 model. In particular, this model is able to match the magnitude and thickness of the wall-jet close to the wall for 2.5 mm downstream of the plasma actuator. Further downstream, a reduced shape by roughly 10% can be observed for the S&H05 model by comparison with the experimental data. The two other models are giving less satisfactory results. The model S&H05 is therefore going to be used for the drag reduction investigations in a turbulent channel flow.

3. Streamwise-aligned plasma actuators in turbulent channel flows

3.1. Uncontrolled channel flow

A turbulent channel flow simulation with no plasma actuators is first generated and will act as the uncontrolled case. Corresponding statistics associated with the simulations of Moser et al. (1999) are presented for comparison. In the reference calculation, pseudo-spectral methods are used with $n_x \times n_y \times n_z = 128 \times 129 \times 128$ de-aliased modes to discretize a computational domain of $L_x \times L_y \times L_z = 4\pi h \times 2h \times 4\pi h/3$ for a nominal value of $h^+ = 180$ where superscript $^+$ indicates a conventional scaling based on the friction velocity u_τ and the kinematic velocity ν. h corresponds to half the height of the channel. For the reference data, the exact value is $h^+ = 178.1$ while the Reynolds number based on the bulk velocity is $Re = U_b h/\nu = 2793$. For our calculation, the same computational domain is used while a constant longitudinal mean pressure gradient is imposed to also reach the nominal value of $h^+ = 180$. A grid of $n_x \times n_y \times n_z = 128 \times 129 \times 256$ mesh nodes is used in the present study. Less mesh nodes could be used in the z-direction, but a fine resolution is needed for an accurate representation of the spanwise-orientated jets generated by the plasma actuators. A stretching is applied in the y-direction to concentrate mesh nodes near the walls at $y = \pm h$, with the first adjacent node to the wall at $y^+ = 1$. All calculations in this study are performed using the same time step $\Delta t = 0.005 h/U_b$. Periodic boundary conditions are used in the x-direction and z-direction while no-slip boundary conditions are imposed at the two walls for $y = \pm h$. Compared with the reference data of Moser et al. (1999), mean and rms velocity profiles are found to be in excellent agreement for the

[1] see www.incompact3d.com .

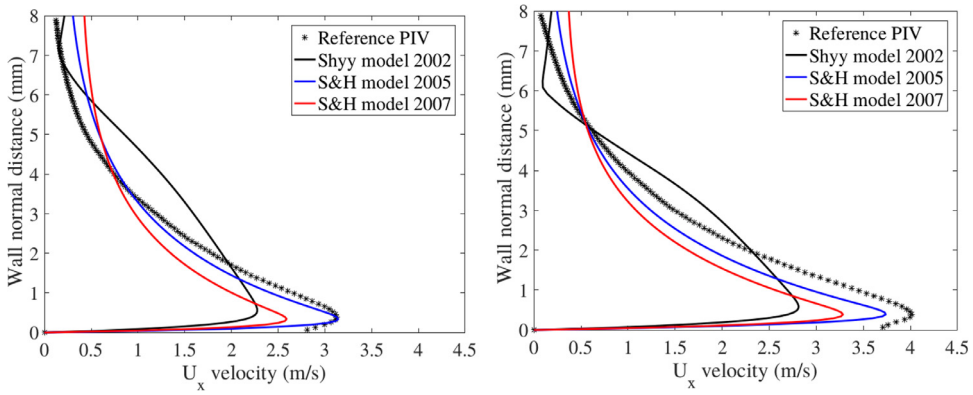

Fig. 5. Comparison between the different models for the time-averaged velocity profile U_x at 2.5 mm and 10 mm downstream of the end of the upper electrode.

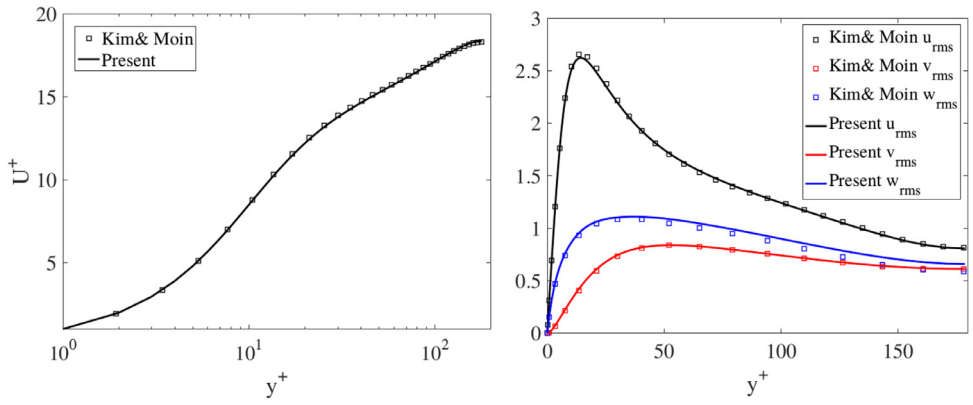

Fig. 6. Comparison of the mean (left) and rms (right) velocity profiles with the data of Moser et al. (1999) for a turbulent channel flow at $Re_\tau = 180$.

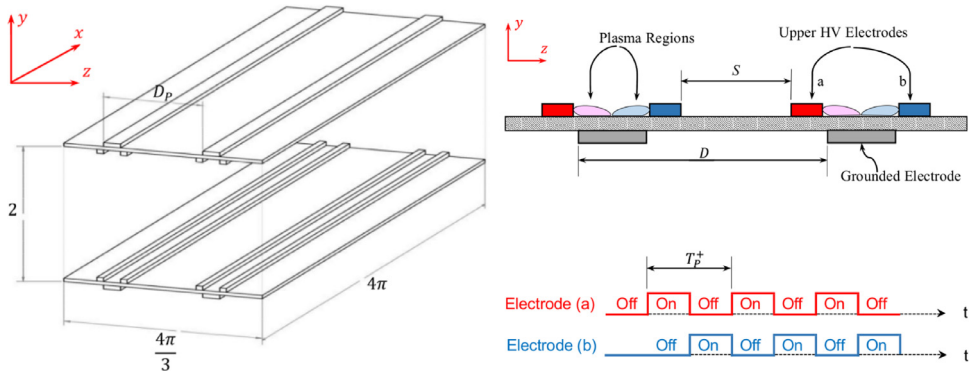

Fig. 7. Left: Sketch of the plasma actuators display for the controlled channel flow simulations (not to scale). Right: Sketch of the cross section of the plasma actuators arrangement (top) and shape of the applied power signal (bottom).

present simulation, as it can be seen in Fig. 6. We can therefore be confident to capture the finest scales of the flow near the walls.

3.2. Controlled channel flow set-up

The streamwise-aligned plasma actuators are distributed on the upper and the lower wall of the channel as seen in Fig. 7 (left). The idea is to create wall-normal spanwise-orientated jets in a similar fashion to the experiments of Jukes et al. (2006), Choi et al. (2011) and Whalley and Choi (2014), but with a sparse display of actuators. Each pair of actuators consists of two exposed electrodes and one common embedded electrode as seen in Fig. 7 (top right) where a cross-section of the actuators is presented. In operation, the power is delivered to the exposed electrodes with the sequence shown in Fig. 7 (bottom right). The objective is to mimic the effect of transverse wall oscillations by using streamwise-aligned pairs of plasma actuators. It was reported in Pang and Choi (2004) that the optimum maximum velocity in wall units should be $w^+_{\max} \approx 10$ for spanwise-orientated jets in order to maximise the potential for drag reduction. In the same study, it was also hypothesized that 20 viscous length is the optimum value for the Lorentz force depth used to generate oscillations near the wall. In our turbulent channel flow at $Re_\tau = 180$, it corresponds to the location of the peak for the time-averaged vertical and spanwise vorticity as seen in Fig. 11 of Laizet and Lamballais (2009).

Getting close to these values can be achieved by applying a 1/5 scaling to the dimensions of the plasma actuator of Fig. 2 which was used for the calibration of the plasma models. When downsizing the plasma actuator by a factor five, the maximum velocity of the jet generated by the actuator is equal to $w^+ = 9.5$ in wall

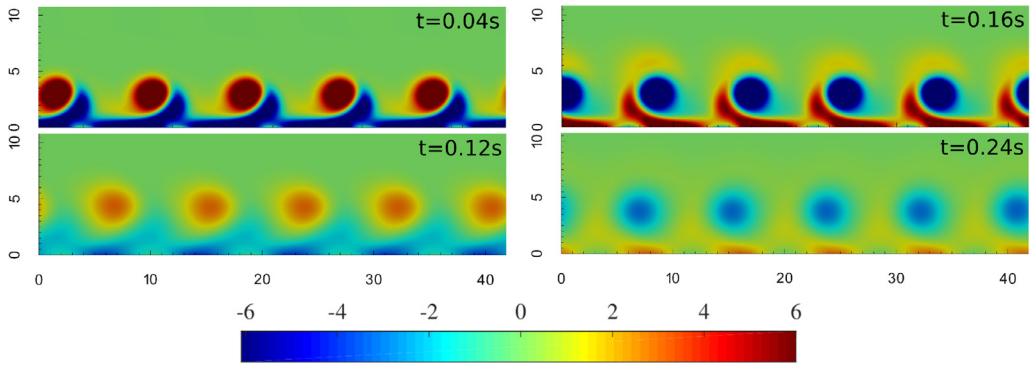

Fig. 8. Formation of vorticity in a fluid at rest generated by opposing pairs of streamwise-aligned plasma actuators with $D_P^+ = 40, T_P^+ = 100$ and $\Delta_P^+ = 10$ corresponding to $D_P = 8$ mm, an oscillating frequency of 4.25 Hz and $\Delta_P = 2$ mm. Dimensions are in mm.

units (normalised using u_τ and the kinematic viscosity ν), maximising the potential for drag reduction. It is similar to the values obtained in the experiments of Jukes et al. (2006), Choi et al. (2011) and Whalley and Choi (2014) where values of $w^+ = 10 - 15$ were reported to maximise the potential for drag reduction. Furthermore, the force height Δ_P^+, defined as the distance from the wall where the force strength drops to lower than 5% of the maximum, is equal to about 20 wall units with a 1/5 scaling, corresponding to the location of very high levels of the time-averaged vertical and spanwise vorticity. The oscillation period for spanwise oscillations for which the potential for drag reduction is higher was reported to be equal to $T^+ \approx 100$ for moderate Reynolds numbers (Jung et al., 1992). With a similar set-up to the present study, a drag reduction of about 45% was achieved in the experiments of Jukes et al. (2006), Choi et al. (2011) and Whalley and Choi (2014) with $T^+ = 16$. Note finally that, in our set-up, T_P^+ is defined as the frequency of the applied power signal as described in Fig. 7. It has no connection with the frequency f_{AC} which is the internal applied voltage frequency of a plasma actuator.

All simulations for the controlled channel flow are initiated from a fully turbulent state obtained in the uncontrolled channel flow simulation. All the statistics presented in the following, collected over $T^+ = 3800$, are obtained after a transitional period during which the flow is adapting to the plasma actuators. The data are normalised in wall units using u_τ from each simulation and the kinematic viscosity ν.

3.3. Spanwise oscillations in a fluid at rest

Fig. 8 presents flow visualizations of the induced flow by the oscillatory plasma actuators in a fluid initially at rest. The results are obtained for $D_P^+ = 40$, $T_P^+ = 100$ and $\Delta_P^+ = 10$ and can be compared with the experimental fog visualisations of Jukes et al. (2006). When the red plasma actuators in Fig. 7 are turned on, counter-clockwise rotating vortices are created. They are known as starting vortices (Whalley and Choi, 2012), they are travelling in the spanwise direction to the right as seen in the first two frames of Fig. 8 and their centres are located at $y^+ \approx 20$. It corresponds to the location of the quasi-streamwise vortices which are responsible for skin-friction drag. Then when the opposing blue plasma are turned on, clockwise-rotating vortices are created, driven this time by wall jets in the spanwise direction to the left as seen in the last two frames of Fig. 8. The first starting vortices rotate around the second starting vortices. The spanwise flow oscillation is thus created by repeating this cycle, with a complex interplay between new and old vortices. As a consequence, the streamwise velocity is expected to be reduced near the wall with either a stretching or the splitting of the large-scale quasi-streamwise vortices.

4. Parametric study to achieve drag reduction

The quantity of main interest in this study is the skin-friction drag coefficient

$$C_f = \frac{2\tau}{\rho U_b^2}$$

where ρ is the density of the fluid (constant in our simulations), τ is the streamwise component of the shear stress at the wall, and U_b is the bulk velocity. The drag reduction DR can be expressed as a percentage of the no-control skin-friction value

$$DR = 100 \times \frac{C_{f,0} - C_f}{C_{f,0}}$$

where the subscript 0 indicates the uncontrolled case. Negative DR values indicates skin-friction increase. Positive DR values correspond to an increase of the flow rate by comparison to the uncontrolled case with a reduction of the streamwise component of the shear stress at the wall (in the present investigations, a constant pressure gradient is imposed for each simulation). We also conducted a temporal convergence study for DR in order to evaluate the accuracy of the results. When doubling the collection time for the statistics from $T^+ = 3800$ to $T^+ = 7600$, DR is only changing by less than 1%. We are therefore confident that the accuracy error of the reported percentages in the following are of the order of 1%.

In Jukes et al. (2006), Choi et al. (2011) and Whalley and Choi (2014), skin-friction drag reduction was achieved in a turbulent boundary layer by applying a spanwise oscillation in the near-wall region of a turbulent boundary layer at a moderate Reynolds number $Re_\tau = 380$. Skin-friction drag was reduced by up to 45% for a frequency of $T_P^+ = 16$ and with a spanwise spacing between the plasma actuators equal to $D_P^+ = 20$. With these parameters in mind and using a small forcing depth of $\Delta_P^+ = 10$ (with a finer resolution in the spanwise direction $n_z = 512$) and the S&H05 model, it is possible to reduce the drag by 38% in our turbulent channel flow set-up with $Re_\tau = 180$. It is a quite convincing result, even if the resulting drag reduction is a bit smaller than the one observed in the experimental data. Note that the experiments were carried out with different plasma actuators and in a turbulent boundary layer with a slightly higher Reynolds number.

However, our aim in this study is to investigate if such drag reduction can be achieved by drastically increasing the distance D_P^+ between two pairs of streamwise-aligned plasma actuators. In the following we focus on D_P^+ ranging from 125 to 754, at least one order of magnitude larger than the spacing in the experiments of Jukes et al. (2006), Choi et al. (2011) and Whalley and Choi (2014). We also investigate the influence of two other parameters: the plasma force height Δ_P^+ and the force oscillation period T_P^+.

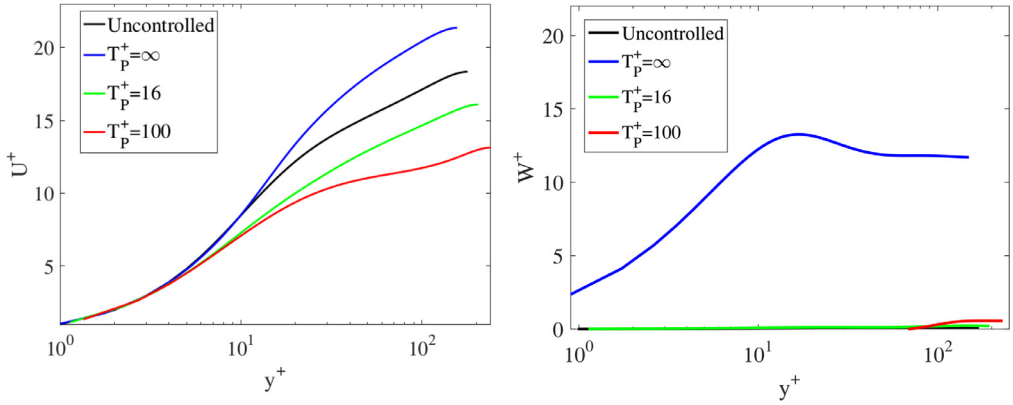

Fig. 9. Time-averaged streamwise velocity profiles (left) and spanwise velocity profiles (right) obtained for $D_P^+ = 378$, $\Delta_P^+ = 20$ and $T_P^+ = 16, 100, \infty$.

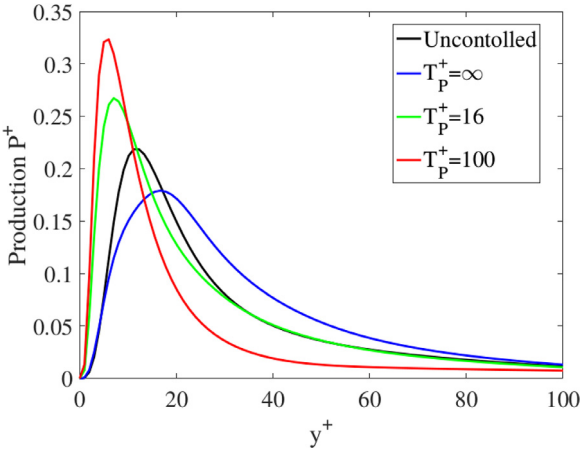

Fig. 10. Time-averaged production profiles obtained for $D_P^+ = 378$, $\Delta_P^+ = 20$ and $T_P^+ = 16, 100, \infty$.

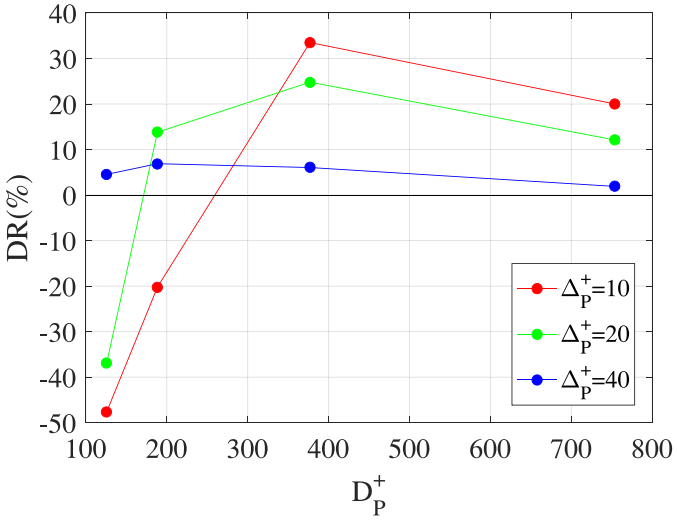

Fig. 11. Dreg reduction for different spanwise spacing (D_P^+) and force height (Δ_P^+).

4.1. Influence of the oscillation frequency

Three oscillation frequencies are considered here, $T_P^+ = 16, 100$ and $T_P^+ = \infty$, ∞ corresponding to a case with no oscillations. For $T_P^+ = \infty$, only the actuator related to the red electrode in Fig. 7 is active (it is on constantly), the actuator related to the blue electrode being always off. The other parameters are a spanwise spacing between pairs of actuators equal to $D_P^+ = 378$ (twenty time less actuators by comparison to the experiments of Jukes et al. (2006), Choi et al. (2011) and Whalley and Choi (2014)) and $\Delta_P^+ = 20$. It is found that with $T_P^+ = 16, 100$ the drag is increased by 29% and 75%, respectively, whereas a drag reduction of 24% is observed for $T_P^+ = \infty$.

Fig. 9 (left) shows the associated normalized (with u_τ and ν from each simulation) time-averaged streamwise velocity profiles in comparison to the uncontrolled case. Close to the wall, the mean streamwise velocity profiles collapse into a single curve but then they deviate in the buffer and the logarithmic regions. Moving up from the velocity profile of the uncontrolled case (black line) means lower shear stress and vice versa. For $T_P^+ = 100$, the curve is distorted from a logarithmic law, as a result of an extensive promotion of turbulent vortices near the wall. Fig. 9 (right) shows that there is virtually no induced spanwise velocity when the oscillation frequency for the plasma actuators is not zero. As expected for the case with $T_P^+ = \infty$ (no oscillation), it can be seen that a substantial spanwise velocity is generated by the plasma actuators as a result of an asymmetric forcing.

The normalized production of turbulent kinetic energy P^+ is presented in Fig. 10. When the drag is increased by 75% (for $T_P^+ = 100$) the peak of P^+ grows by 43% by comparison to the uncontrolled case, and the peak is shifted from 12 wall units to 6 wall units from the wall. When the drag is decreased ($T_P^+ = \infty$), the maximum production is lowered by 19% by comparison to the uncontrolled case and the peak is located at 16 wall units from the wall. When the production grows closer and closer to the wall, high levels of turbulent kinetic energy near the wall are increasing the shear stress and the skin-friction drag. It seems that when D_P^+ is very large and for our particular pairs of plasma actuators, significant skin-friction drag reduction can only be achieved with no oscillations, corresponding to a unidirectional spanwise-orientated forcing. The main question now is to see if it is possible to further increase the drag reduction by optimising the parameters D_P^+ and Δ_P^+ when $T_P^+ = \infty$.

4.2. Influence of the actuators spacing and the force penetration height

Fig. 11 illustrates how DR vary with respect to D_P^+ and Δ_P^+ when $T_P^+ = \infty$. It can be seen that the highest skin-friction drag reduction is obtained for $D_P^+ = 378$ and $\Delta_P^+ = 10$ with $DR = 33\%$. When the distance between two actuators is small ($D_P^+ = 125$) the skin-friction drag can actually be increased. When D_P^+ is very large, drag reduction can be obtained but with $DR < 20\%$. The spacing be-

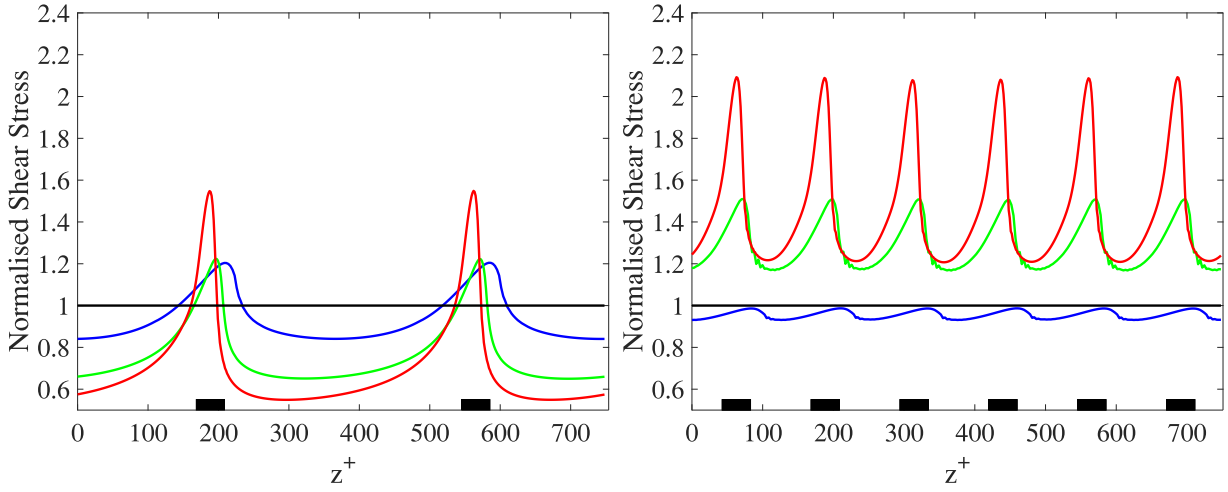

Fig. 12. Spanwise distribution of the time-averaged streamwise-averaged shear stress for $D_P^+ = 378$ (left) and for $D_P^+ = 125$ (right). The black rectangles indicate the location of the actuators.

tween actuators is critical to achieve significant skin-friction drag reduction. The main result here is that with a sparse array of actuators (twenty times less plasma actuators than in the experiments of Jukes et al. (2006), Choi et al. (2011) and Whalley and Choi (2014)), it is still possible to reduce the skin-friction drag.

Fig. 12 shows time-averaged and streamwise-averaged wall shear stress profiles for $D_P^+ = 378$ and for $D_P^+ = 125$. The black rectangles correspond to the position of the actuators. The black line corresponds to the time-averaged and streamwise-averaged shear stress for the uncontrolled case. When the plasma actuators are activated, a downwash occurs between the electrodes, as the plasma entrains fluid from above it to replace the fluid ejected in the spanwise direction. As a result, peaks on the wall shear stress can be observed just above the electrodes. Note also that the small asymmetry of the profiles as the plasma actuators are only working in one direction. It seems to suggest that the spanwise induced flow by the plasma actuators observed in Fig. 9 (right) does not affect too much the streamwise-averaged wall shear stress profiles. When drag reduction is achieved for $D_P^+ = 378$, it can be seen that the wall shear stress can be reduced by up to 45% between the actuators (red line) whereas it is increased by 60% just above the actuators ($DR = 33\%$ in average). Interestingly, when the distance between the actuators is reduced ($D_P^+ = 125$), the overall level for the shear stress is much higher, especially for $\Delta_P^+ = 10$ resulting in a significant drag increase.

4.3. Turbulent structures

In this section, we focus on the coherent structures at the wall in order to get a better idea on the drag reduction and increase observed in the previous section. It is well-known that the streaks are large-scale elongated structures in the streamwise direction of the flow consisting of negative/positive streamwise velocity perturbations, with localized regions of decelerated/accelerated flow. Those streaks can clearly be seen in Fig. 13 (top) for the uncontrolled flow. They are evenly distributed and aligned with the streamwise direction, with an average distance between them of about 100–125 viscous lengths. When the plasma actuators are active, two scenarios can happen: either very intense high-speed streaks are promoted as seen in the bottom left frame of Fig. 13 or high-speed events are destroyed as seen in the bottom right frame of Fig. 13. In the first situation, the strength of the more intense streaks is amplified by $\approx$ 45% with two massive streaks located above the actuators. Between the actuators, the streaks are very similar to the ones observed in the uncontrolled case. As a result, the skin-friction drag is considerably increased. In the second situation, the high-speed events are almost completely destroyed and the skin-friction drag is reduced.

Fig. 14 presents instantaneous snapshots of the vorticity magnitude for the same three cases studied in Fig. 13. For the first scenario, it can be seen that the number of intense vortical structures has been increased significantly by comparison to the uncontrolled case. It can explain why the time-averaged shear stress has been increased by 75% for this scenario. On the contrary, far less intense structures can be observed in the second scenario, and the flow is probably "less turbulent" than for the uncontrolled case. In the near-wall region of turbulent flows, low-speed fluid is intermittently ejected away from the wall. Such process contributes to the production of turbulence with the creation of hairpin vortices, characterized by a transverse vortex forming the head and one or two-legged vortex (Kline et al., 1967; Corino and Brodkey, 1969). Strong ejections occur upstream of the vortex hairpin head, while sweeps are found on the downstream side. A shear layer separates ejection and sweep events. An ejection is a low-velocity fluid event moving away from the wall whereas a sweep is a high-speed event moving toward the wall (Kline et al., 1967; Corino and Brodkey, 1969). Ejections and sweeps are considered to be principal contributors to shear stress and are responsible for skin-friction drag. It can be hypothesized that less sweeps and ejections are present in the second scenario and that skin-friction drag reduction can be achieved as a result.

4.4. VITA analysis

The Variable Interval Time Averaging (VITA) technique (Blackwelder and Kaplan, 1976), based on conditional samplings, can be used to study the modification of the near-wall structures as a result of the use of the plasma actuators. Using virtual probes at various locations from the wall, it is possible to collect single-point time signals of the streamwise velocity in a similar fashion to what is done experimentally with hot-wire probes. Following the VITA study in Jukes et al. (2006), Choi et al. (2011) and Whalley and Choi (2014), the window length T_{win}^+ over which the local variance is calculated is set to $T_{win}^+ = 10$, with a selective detection of events with positive velocity gradient (with respect to time). Only the events with a variance larger than the u_{rms} of the total time signal and with $du/dt > 0$ are detected (the threshold parameter k is equal to 1, as suggested in Jukes et al., 2006; Choi et al., 2011; Whalley and Choi, 2014). It corresponds

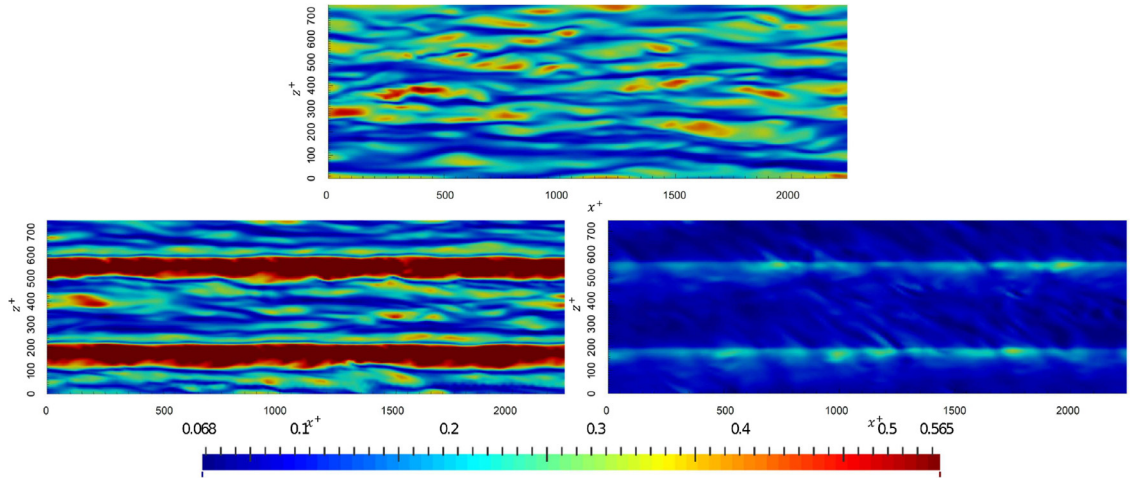

Fig. 13. Instantaneous streamwise velocity contour in x-z plane at $y^+ = 5$ that shows the streaks of four cases. The colour bar scale is normalized by mean streamwise velocity, and its limits are the maximum and minimum values of the uncontrolled flow. The top frame corresponds to the uncontrolled case, the bottom left frame to the simulation with $DR = -75\%$ ($D_p^+ = 376$, $T_p^+ = 100$ and $\Delta_p^+ = 10$) and the bottom right frame to the simulation with $DR = 33\%$ ($D_p^+ = 376$, $\Delta_p^+ = 10$ and $T_p^+ = \infty$).

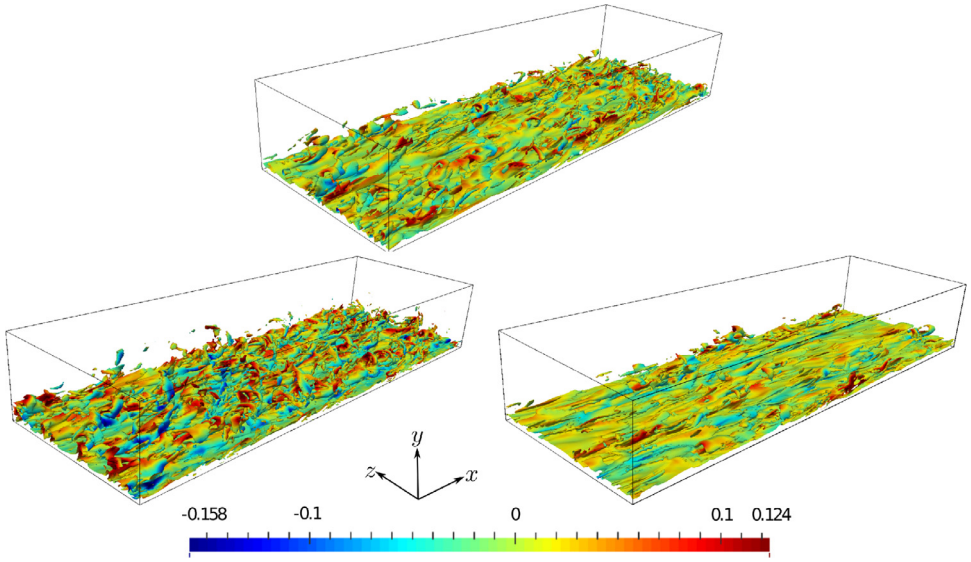

Fig. 14. Instantaneous visualization of the isosurface $|\omega| = 0.325(u_\tau^2/\nu)$ of the vorticity magnitude, coloured by the wall normal velocity normalized by the mean streamwise velocity. The top frame corresponds to the uncontrolled case, the bottom left frame to the simulation with $DR = -75\%$ ($D_p^+ = 376$, $T_p^+ = 100$ and $\Delta_p^+ = 10$) and the bottom right frame to the simulation with $DR = 33\%$ ($D_p^+ = 376$, $\Delta_p^+ = 10$ and $T_p^+ = \infty$).

to events which transport high-speed fluid towards the wall (e.g. sweeps). According to Kravchenko et al. (1993) and Orlandi and Jiménez (1994), the sweeps are responsible for the majority of the skin-friction drag close to the wall.

The time series of the streamwise velocity fluctuations at $y^+ = 5$ and $y^+ = 20$ for the uncontrolled channel flow and for the channel flow for with $DR = 33\%$ are shown in Fig. 15. They are collected at $z^+ = 378$ corresponding to the middle point between two actuators. It can be seen that close to the wall for $y^+ = 5$, the amplitude of the fluctuations is significantly reduced when the plasma actuators are in use by comparison to the uncontrolled case. This trend is different than the one observed in Jukes et al. (2006), Choi et al. (2011) and Whalley and Choi (2014) where large positive spikes were observed in a boundary layer with oscillating streamwise-aligned pairs of plasma actuators. Further away from the wall (at $y^+ = 20$), it seems that the frequency of the fluctuations has been increased for the control case, with also a less intermittent signal.

Fig. 16 shows that the characteristic signature of a sweep event is recovered for the uncontrolled case, with a very similar shape to the one obtained in the experiments of Jukes et al. (2006), Choi et al. (2011) and Whalley and Choi (2014). It can be seen that when the plasma actuators are active, the sweeps are destroyed, as already suggested by the 2D maps of streamwise velocity in Fig. 13. Basically, the events which transport high-speed fluid towards the wall have been removed, with a significant drag reduction as a result. It is a different mechanism that the one observed in Jukes et al. (2006), Choi et al. (2011) and Whalley and Choi (2014), where sweeps are still present when the plasma actuators are active, but with a reduced duration, strength and intensity. It is now well established that the physics of near-wall turbulence is based on a self-sustaining (or regeneration) process (Offen and Kline, 1975; Robinson, 1991; Jiménez and Pinelli, 1999; Schoppa and Hussain, 2002; Kim, 2011). It involves the formation of velocity streaks from the advection of the mean profile by streamwise vortices, and the generation of the vortices from the instability of the streaks. It has now been recognized, thanks to numerical investigations, that it is the streamwise vortices that are mainly responsible for skin-friction drag, at least for low Reynolds numbers

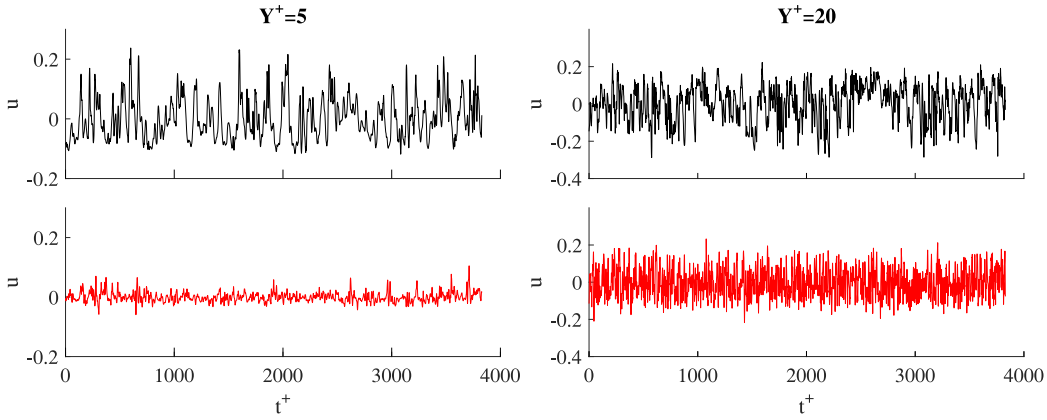

Fig. 15. Time series of the streamwise velocity fluctuations (obtained at $z^+ = 378$) for $y^+ = 5$ (top) and $y^+ = 20$ (bottom) for the uncontrolled channel flow (black lines) and for the channel flow for with $DR = 33\%$ (red lines). (For interpretation of the references to colour in this figure legend, the reader is referred to the web version of this article.)

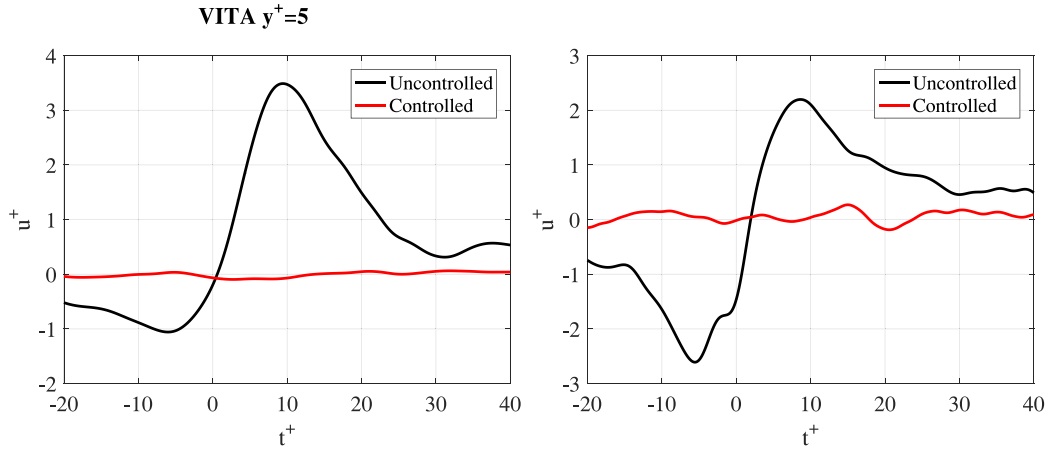

Fig. 16. VITA-detected sweep events at $y^+ = 5$ (top) and $y^+ = 20$ (bottom) for the uncontrolled channel flow (black lines) and for the channel flow for with $DR = 33\%$ (red lines). (For interpretation of the references to colour in this figure legend, the reader is referred to the web version of this article.)

flows. Any alteration of the cycle could potentially result in skin-friction drag reduction. In our study, it is hypothesised that the spanwise motion induced by the plasma actuators are disrupting or even cancelling the quasi-streamwise vortices at the wall, thus modifying the whole turbulence regeneration cycle. Furthermore, it is also suggested that the creation and development of the hairpin vortices is inhibited by the induced spanwise jets such that sweep events cannot occur any more. This leads to a reduction of the wall shear stress and associated skin-friction drag.

4.5. Power balance

One important issue with active control solutions such as plasma actuators is the additional power input require to manipulate the flow. The key factor for an efficient active control solution is that the energy saved as a consequence of skin-friction drag reduction is larger than the input power for the active control solution. It is well-known that the efficiency of plasma actuators, measured as the ratio of the mechanical power to the electrical power is still quite small, of the order of 0.1% (Giepman and Kotsonis, 2011). It means that only 0.1% of the electrical energy consumed by the actuator(P_E) is converted to kinetic energy in the flow(P_f).

Although it can be interesting to analyse plasma actuators from the point of view of its mechanical efficiency, it is not the only measure of efficiency. For active flow control solutions, the main question is how effective it is in improving beneficial effects and/or in reducing negative effects of the turbulence. In that role it was demonstrated in this numerical study that significant drag reduction can be achieved, even if the mechanical efficiency is very low. It is hoped that in the next few years the efficiency of plasma actuators will be increased by one or two order of magnitude. Assuming an idealised situation for which a plasma actuator can convert all the electrical power into kinetic energy for the flow, the effectiveness of the control can be based on the energy transfer to the flow rather than to the actual electrical energy. P_f can be calculated in a quiescent fluid with the following equation introduced by (Giepman and Kotsonis, 2011)

$$P_f = \int_\Omega \mathbf{f} \cdot \mathbf{u} d\Omega \tag{16}$$

where $\mathbf{f}$ is the body force applied by the plasma on the flow, $\mathbf{u}$ is the flow velocity and Ω is a volume that contains the plasma force. Then it is possible to evaluate the pumping power $P_t = VR \times \Delta P$ required to overcome the shear stress at the wall with VR defined as the volume flow rate and ΔP as the pressure drop between the inlet and outlet of the channel. The ideal net power saved P_s by the streamwise-aligned plasma actuators can be expressed as

$$P_s = \frac{\Delta P_t - P_f}{P_t} \tag{17}$$

where ΔP_t is the difference of pumping power between the uncontrolled case and the control case.

Fig. 17 shows the percentage of ideal net power saved for different spanwise spacings and force heights in our simulations. Negative values means that the control power P_f is larger than the

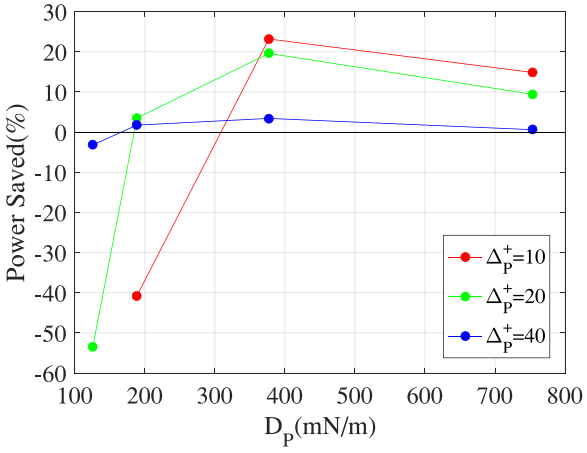

Fig. 17. Ideal power saved for various spanwise spacings and force heights.

saved power by drag reduction. In this idealized context, the total energy cut can be as high as 23%. Therefore, when the electrical efficiency of plasma actuators will be improved, a sparse array of streamwise-aligned plasma actuators could be an efficient solution for skin-friction drag reduction.

5. Conclusion

High-fidelity simulations of a turbulent channel flow at a moderate Reynolds number were carried out to investigate the potential for skin-friction drag reduction using streamwise-aligned plasma actuators. The idea is to generate wall-normal spanwise-orientated jets close to destroy high-speed large-coherent structures responsible for skin-friction drag. By comparison to similar experiments, the objective was to drastically increase the spacing between the actuators in order to reduce the input power required for this active flow control solution. In order to model the effect of the plasma actuators, three simple phenomenological models were tested and confronted with experimental PIV data. It was found that the S&H05 model (Suzen et al., 2005) was the best match to mimic the effect of the plasma actuator considered in this numerical study. The influence of various parameters was investigated: the force magnitude, the force height, the oscillating frequency, and the spanwise distance between actuators. The main results and conclusions are summarised as follow:

- In a turbulent channel flow and for a sparse array of actuators, a periodic forcing generates vortical structures that can promote drag, with an increase of up to 75%. However, when the forcing is applied in one direction only, it is possible to achieve substantial drag reduction, up to 33%.
- Previous experimental studies (Jukes et al., 2006; Choi et al., 2011; Whalley and Choi, 2014) demonstrated that it is possible to achieve drag reduction with a very dense array of streamwise-aligned plasma actuators. We demonstrated that it is also possible to achieve drag reduction with a sparse array of streamwise-aligned plasma actuators, with one order of magnitude less actuators than in the experiments.
- The actuator size, the height and the frequency of oscillations are key parameters in order to achieve drag reduction.
- Drag reduction was achieved by removing the events which transport high-speed fluid towards the wall.
- DBD plasma actuators have a high electrical energy consumption that over rid the saved power from the skin-friction drag reduction. However, if an efficient design of DBD plasma actuators is found, then theoretically power saving is possible (up to 23%).

Acknowledgement

Sylvain Laizet would like to thank EPSRC for its financial support (EP/M022676/1) and for the computational time made available on the UK supercomputing facility ARCHER via the UK Turbulence Consortium (EP/L000261/1). Finally, the authors would like to acknowledge the NATO Applied Vehicle Technology (AVT) 254 “Assessment of Plasma Actuator Technologies for Internal Flows”.

References

Baron, A., Quadrio, M., 1995. Turbulent drag reduction by spanwise wall oscillations. Appl. Sci. Res. **55(4)**, 311–326.
Benard, N., Caron, M., Moreau, E., 2015. Evaluation of the time-resolved EHD force produced by a plasma actuator by particle image velocimetry–a parametric study. J. Phys. **646(1)**, 12055–12058.
Berger, T., Kim, J., Lee, C., Lim, J., 2000. Turbulent boundary layer control utilizing the Lorentz force. Phys. Fluids **12(3)**, 631–649.
Blackwelder, R., Kaplan, R., 1976. On the wall structure of the turbulent boundary layer. J. Fluid Mech. **76(01)**, 89–112.
Boeuf, J., Lagmich, Y., Unfer, T., Callegari, T., Pitchford, L., 2007. Electrohydrodynamic force in dielectric barrier discharge plasma actuators. J. Phys. D **40(3)**, 652.
Bradshaw, P., Pontikos, N., 1985. Measurements in the turbulent boundary layer on an infinite swept wing. J. Fluid Mech. **159**, 105–130.
Capitelli, M., Ferreira, C., Gordiets, B., Osipov, A., 2013. Plasma Kinetics in Atmospheric Gases, **31**. Springer Science & Business Media.
Choi, J., Xu, C., Sung, H., 2002. Drag reduction by spanwise wall oscillation in wall-bounded turbulent flows. AIAA J. **40(5)**, 842–850.
Choi, K.-S., DeBisschop, J.-R., Clayton, B., 1998. Turbulent boundary-layer control by means of spanwise-wall oscillation. AIAA J. **36(7)**, 1157–1163.
Choi, K.-S., Jukes, T., Whalley, R., 2011. Turbulent boundary-layer control with plasma actuators. Philos. Trans. R. Soc. London A **369(1940)**, 1443–1458.
Corino, E., Brodkey, R., 1969. A visual investigation of the wall region in turbulent flow. J. Fluid Mech. **37(01)**, 1–30.
Corke, T., Enloe, C., Wilkinson, S., 2010. Dielectric barrier discharge plasma actuators for flow control. Ann. Rev. Fluid Mech. **42**, 505–529.
Du, Y., Symeonidis, V., Karniadakis, G., 2002. Drag reduction in wall-bounded turbulence via a transverse travelling wave. J. Fluid Mech. **457**, 1–34.
Giepman, R., Kotsonis, M., 2011. On the mechanical efficiency of dielectric barrier discharge plasma actuators. Appl. Phys. Lett. **98(22)**, 221504.
Ibrahim, I., Skote, M., 2014. Simulating plasma actuators in a channel flow configuration by utilizing the modified Suzen–Huang model. Comput. Fluids **99**, 144–155.
Iwamoto, K., Fukagata, K., Kasagi, N., Suzuki, Y., 2005. Friction drag reduction achievable by near-wall turbulence manipulation at high Reynolds numbers. Phys. Fluids **17(1)**. 011702–011702.
Iwamoto, K., Suzuki, Y., Kasagi, N., 2002. Reynolds number effect on wall turbulence: toward effective feedback control. Int. J. Heat Fluid Flow **23(5)**, 678–689.
Jiménez, J., Pinelli, A., 1999. The autonomous cycle of near-wall turbulence. J. Fluid Mech. **389**, 335–359.
Jukes, T., Choi, K.-S., Johnson, G., Scott, S., 2006. Turbulent drag reduction by surface plasma through spanwise flow oscillation. AIAA Paper **2006–3673**.
Jung, W., Mangiavacchi, N., Akhavan, R., 1992. Suppression of turbulence in wall-bounded flow by high-frequency spanwise oscillations. Phys. Fluids A **4(8)**, 1605–1607.
Kim, J., 2011. Physics and control of wall turbulence for drag reduction. Philos. Trans. R. Soc. London A **369** (1940), 1396–1411.
Kline, S., Reynolds, W., Schraub, F., Runstadler, P., 1967. The structure of turbulent boundary layers. J. Fluid Mech. **30(4)**, 741–773.
Kravchenko, A., Choi, H., Moin, P., 1993. On the relation of near-wall streamwise vortices to wall skin friction in turbulent boundary layers. Phys. Fluids A **5(12)**, 3307–3309.
Laizet, S., Lamballais, E., 2009. High-order compact schemes for incompressible flows: a simple and efficient method with the quasi-spectral accuracy. J. Comput. Phys. **228(16)**, 5989–6015.
Li, Z., Hu, B., Lan, S., Zhang, J., Huang, J., 2015. Control of turbulent channel flow using a plasma-based body force. Comput. Fluids **119**, 26–36.
Mertz, B., Corke, T., 2011. Single-dielectric barrier discharge plasma actuator modelling and validation. J. Fluid Mech. **669**, 557–583.
Moin, P., Shih, T., Driver, D., Mansour, N., 1990. Direct numerical simulation of a three-dimensional turbulent boundary layer. Phys. Fluids A **2(10)**, 1846–1853.
Moreau, E., 2007. Airflow control by non-thermal plasma actuators. J. Phys. D **40(3)**, 605.
Moser, R.D., Kim, J., Mansour, N.N., 1999. Direct numerical simulation of turbulent channel flow up to $Re_\tau = 590$. Phys. Fluids **11(4)**, 943–945.
Nishida, H., Nonomura, T., Abe, T., 2014. Three-dimensional simulations of discharge plasma evolution on a dielectric barrier discharge plasma actuator. J. Appl. Phys. **115(13)**, 133301.
Nishida, H., Nonomura, T., Abe, T., 2016. Numerical study on spanwise nonuniformity in body-force field of dielectric-barrier-discharge plasma actuator. AIAA J. **54(2)**, 659–669.
Offen, G., Kline, S., 1975. A proposed model of the bursting process in turbulent boundary layers. J. Fluid Mech. **70(2)**, 209–228.

Orlandi, P., Jiménez, J., 1994. On the generation of turbulent wall friction. Phys. Fluids **6(2)**, 634–641.
Pang, J., Choi, K.-S., 2004. Turbulent drag reduction by Lorentz force oscillation. Phys. Fluids **16(5)**, L35–L38.
Parent, B., Shneider, M., Macheret, S., 2016. Detailed modeling of plasmas for computational aerodynamics. AIAA J. **54(1)**, 1–14.
Quadrio, M., Ricco, P., 2004. Critical assessment of turbulent drag reduction through spanwise wall oscillations. J. Fluid Mech. **521**, 251–271.
Ricco, P., 2004. Modification of near-wall turbulence due to spanwise wall oscillations. J. Turbul. **5**. 20–20.
Robinson, S., 1991. Coherent motions in the turbulent boundary layer. Ann. Rev. Fluid Mech. **23(1)**, 601–639.
Rogier, F., Dufour, G., Kourtzanidis, K., 2014. Numerical simulation of sinusoidal driven DBD actuators and comparisons with experiments. AIAA Paper **2014–2808**.
Roth, J.R., 1995. Industrial Plasma Engineering: Volume 1-Principles, **1**. CRC press.
Schoppa, W., Hussain, F., 2002. Coherent structure generation in near-wall turbulence. J. Fluid Mech. **453**, 57–108.
Segawa, T., Mizunuma, H., Murakami, K., Li, F.-C., Yoshida, H., 2007. Turbulent drag reduction by means of alternating suction and blowing jets. Fluid Dyn. Res. **39(7)**, 552–568.
Shyy, W., Jayaraman, B., Andersson, A., 2002. Modeling of glow discharge-induced fluid dynamics. J. Appl. Phys. **92(11)**, 6434–6443.
Singh, K.P., Roy, S., 2008. Force approximation for a plasma actuator operating in atmospheric air. J. Appl. Phys. **103(1)**, 013305.
Suzen, Y., Huang, P., Ashpis, D., 2007. Numerical simulations of flow separation control in low-pressure turbines using plasma actuators. AIAA Paper **2007-937**.
Suzen, Y., Huang, P., Jacob, J., Ashpis, D., 2005. Numerical simulations of plasma based flow control applications. AIAA Paper **2005–4633**.
Tardu, S., 2001. Active control of near-wall turbulence by local oscillating blowing. J. Fluid Mech. **439**, 217–253.
Touber, E., Leschziner, M., 2012. Near-wall streak modification by spanwise oscillatory wall motion and drag-reduction mechanisms. J. Fluid Mech. **693**, 150.
Virk, P., 1975. Drag reduction fundamentals. AlChE J. **21(4)**, 625–656.
Whalley, R., Choi, K., 2012. The starting vortex in quiescent air induced by dielectric-barrier-discharge plasma. J. Fluid Mech. **703**, 192–203.
Whalley, R., Choi, K.-S., 2014. Turbulent boundary-layer control with plasma spanwise travelling waves. Exp. Fluids **55(8)**, 1–16.